Fuel 321 (2022) 124006

Contents lists available at ScienceDirect

Fuel

journal homepage: www.elsevier.com/locate/fuel

Full Length Article

Monitoring flame soot maturity by variable temperature Raman spectroscopy

Mario Commodo [a], Gianluca Serra [b], Serafina Bocchicchio [a], Patrizia Minutolo [a,*], Matteo Tommasini [b,*], Andrea D'Anna [c]

[a] Istituto di Scienze e Tecnologie per l'Energia e la Mobilità Sostenibili, Consiglio Nazionale delle Ricerche, P.le Tecchio 80, 80125 Napoli, Italy
[b] Dipartimento di Chimica, Materiali e Ing. Chimica "G. Natta", Politecnico di Milano, Piazza Leonardo da Vinci 32, 20133 Milano, Italy
[c] Dipartimento di Ingegneria Chimica, dei Materiali e della Produzione Industriale, Università degli Studi di Napoli "Federico II", P.le Tecchio 80, 80125 Napoli, Italy

ARTICLE INFO

Keywords:
Raman spectroscopy
Nanoparticles
Soot maturity
Flames
Carbon
Density functional theory

ABSTRACT

Flame-formed soot nanoparticles are known to possess different nanostructures as a function of a large variety of combustion operative parameters, including particle residence time in flames, flame stoichiometry, fuel chemical composition, temperature and pressure. This implies that important properties (*e.g.*, soot oxidation reactivity, optical and electronic gap) may be different depending on the way soot particles are generated. Hence, it is beneficial to develop diagnostic methods that are sensitive to such differences among the various kinds of soot particles. In this work we investigate by off-line variable-temperature Raman spectroscopy two types of soot particles, namely just-nucleated and aged/mature particles, with a different size and maturity degree. The results obtained for soot particles have been compared and discussed with those found for other related carbon materials. As the Raman spectra are recorded at increasing sample temperature, from 300 to 525 K, both soots display a linear downshift of the position of the two main Raman modes (D and G bands). Just-nucleated soot particles exhibit the strongest temperature dependence of the position of the G band. Based on results from density functional theory calculations, interpreted by a simple empirical model, the observed temperature coefficient differences can be ascribed to differences in the nanostructural order of the two soot samples, which causes a different thermal expansion behavior.

1. Introduction

In fuel-rich combustion systems, oxidative and pyrolytic reactions lead to the formation of a large variety of carbonaceous materials including gas-phase polycyclic aromatic hydrocarbons (PAHs), condensable phase tar-like materials, and solid soot nanoparticles. Soot particle generation is the result of a considerable complex matrix of chemical and physical processes that occurs in a very short timescale of the order of a few milliseconds.

Since long, the formation of carbon particulates in flames has attracted considerable interest from the scientific community because of the detrimental effects, for both human health and for the climate change [1–3], of carbon particulates emitted into the atmosphere. Nevertheless, combustion-generated carbon particles and nanoparticles also found past and recent technological interest for a large variety of applications [4]. Thus, the physicochemical evolution of carbon soot nanoparticles in flames has been extensively investigated over the years, and it is part of an ongoing and considerable research activity.

Soot particles are the result of benzene and gas-phase PAHs formation, particle nucleation, particle growth by coagulation/coalescence and mass addition, carbonization and oxidation [5–9]. During these processes, *i.e.*, from nucleation to the later growing process, soot nanoparticles undergo the most significant modifications: the particle size increases from a few to tens of nanometers [10–13], the particle density increases [16] and the chemical structure is modified, as evidenced by the hydrogen/carbon ratio that starts from 0.5 to 0.4 for just-nucleated, incipient soot particles, and reduces to 0.2–0.1 for the mature or "aged" soot particles [14,15]. Such modifications are also associated to changes in terms of structural order of the aromatic molecular constituents [12,17] and degree of chemical cross linking among aromatics [18]. The evolution from mostly amorphous particles to more ordered or "core–shell" nanostructures becomes evident [15,17]. Because of these modifications, the optical and electronic band gap reduce from approximatively 2–1.5 eV in just-nucleated soot to 0.5–0.3 eV in mature

* Corresponding authors.
E-mail addresses: patrizia.minutolo@stems.cnr.it (P. Minutolo), matteo.tommasini@polimi.it (M. Tommasini).

https://doi.org/10.1016/j.fuel.2022.124006
Received 7 February 2022; Received in revised form 21 March 2022; Accepted 25 March 2022
Available online 31 March 2022

soot particles [19–22]. In addition, the soot reactivity towards oxidation reduces [23].

Given such complexity, the soot formation process and the characteristics of soot particles have been investigated using a large array of techniques. To this end, Raman spectroscopy has become, in the recent years, a common tool for the characterization of combustion-generated carbonaceous soot particles [24–34]. Owning to its high sensitivity to the structural disorder of the carbon material, Raman spectroscopy is particularly useful in discerning and characterizing amorphous and highly disordered carbons, including soot nanoparticles, as well as their evolving properties, as a function of most of the combustion operative parameters. Indeed, Raman spectroscopy has been used, for instance, to correlate soot nanostructure with residence time [12,26], fuel chemistry [25,33], pressure of the combustion system [29,30], flame equivalence ratio [31], flame temperature [34], oxidative reactivity [27] and radical character [32], just to mention a few cases. In addition, through the analysis of the temperature-dependence of the line width and peak shift, Raman spectroscopy is a powerful method to study anharmonic terms in the lattice potential energy and the electron–phonon coupling (EPC) of the corresponding phonons in condensed matter [35]. Studies on phonon anharmonicity are of interest from both a theoretical and a practical point of view. For instance, phonon anharmonicity has been found a dominant part of the effect of interlayer interactions on the in-plane thermal conductivity of bilayer graphene and graphite [36]. As temperature increases, a linear downshift of the frequencies of the Raman peaks is usually observed, in relation with the phonon anharmonic contribution to the lattice potential, and the lengthening of the C–C bonds. Under this regard, temperature-dependent Raman spectra have been already investigated for a large variety of carbon-based materials including, for instance: pyrolytic and glass-like carbon [37], diamond [38], graphite and highly ordered pyrolytic graphite (HOPG) [39–41], multiwall carbon nanotubes (MWCNTs) and activated carbon [42], single-wall carbon nanotubes (SWCNTs) [43,44], double-wall carbon nanotubes (DWCNTs) with different diameters [45], Au-ion implanted (defective) highly oriented pyrolytic graphite (HOPG) [43], graphene, graphene multilayers and graphene quantum dots (GQDs) [46–49], and nano-crystalline carbon/ceramic composites [50]. For most of these materials, the obtained temperature coefficient, χ, corresponding to the slope of the linear fit of the Raman frequencies, in the investigated range of temperature was found between −0.01 and −0.04 cm^{-1}/K.

In this work, to the best of our knowledge, we present the first investigation of the temperature-dependent Raman spectra of soot nanoparticles, with different size and structural characteristics, collected from a laboratory premixed flame. We introduce a simple empirical model, supported by density functional theory (DFT) calculations, to provide the interpretation of the temperature dependence of the Raman G band of soot. The results obtained for the soot particles are also discussed with respect to those obtained from different carbon-based structures and from coronene and fullerene C_{60} powders. The aim is to investigate structural differences in the different kinds of soot particles through their thermal response and provide a proof of concept for the use of this method as a diagnostic tool for the determination of the maturity/graphitization level of soot particles and related or similar carbon materials.

2. Materials and methods

2.1. Flame and sampling conditions

Flame-formed soot nanoparticles were sampled from an ethylene/air laminar premixed flame stabilized on a water-cooled McKenna burner. The cold gas velocity was set to 9.8 cm/s (STP) and the flame equivalence ratio, Φ, was 2.01. Soot samples were collected at two different heights above the burner surface, Z, corresponding to different particle residence times and different soot regions of the flame. A picture of the flame is shown in Fig. 1. Specifically, we collected soot at the height above the burner of $Z = 8$ mm, corresponding to a zone of the flame where just-nucleated soot nanoparticles are present (*i.e.*, they have a very small size with a volume mean diameter $<D>$ of 3.5 nm), and $Z =$ 14 mm, where larger, and more aged/mature soot particles are present, with average size of $<D> = 18.5$ nm. The complete evolution of the soot particle size distribution, measured in the aerosol phase, has been reported and discussed elsewhere [12,22]. Fig. S1, in the Supplementary material, reports the normalized volumetric particle distributions for the two conditions selected in this study.

Soot nanoparticles were sampled using a horizontal tubular probe (stainless steel tube, 1 cm outer diameter) with a downward orifice (inner diameter = 0.2 mm, thickness = 0.5 mm) positioned at the sampling point in the flame through which the aerosol particles entered into the sampling line, as described in earlier contributions [12,31,32]. The sampled aerosol was deposited on a quartz filter (Whatman QM-A Quartz Microfiber Filters, with a diameter of 25 mm) positioned on-line in a filter holder.

Particles collected on the quartz microfiber filter were characterized off-line by *in-situ* Raman spectroscopy, in a range of temperatures spanning from room temperature up to 525 K. To this end, a small piece, about 1 cm^2, of the quartz filter covered by soot particles was cut and positioned inside a programmable heating microscope stage (Mod. Linkam HFS600E-PB4, Linkam Scientific Instruments, UK) without further manipulations. All the experiments were carried out by heating soot in an inert atmosphere of N_2. The heating was programmed with a 15 K/min linear ramp, and a holding time of 10 min at each temperature step of 25 K, necessary for the collection of the Raman spectra. For each temperature step, a few minutes were waited to allow the sample to thermally stabilize before starting the spectroscopic analysis. The same kind of temperature dependent Raman experiments were also carried out on coronene and fullerene-C_{60} powders purchased from Sigma-Aldrich and used without further manipulation.

Raman spectroscopy measurements were performed by positioning the heating stage under the microscope (Mod. XploRA, Horiba, Japan) equipped with a long working distance 50X objective (NA0.5 Olympus, Germany), a Nd:YAG ($\lambda_{exc} = 532$ nm, 12 mW maximum laser power) and a 200 μm pinhole for confocal photons collection. The wavenumber calibration was performed against the Stokes Raman signal of pure silicon (520 cm^{-1}). The power of the excitation laser beam was attenuated to 1% to avoid structural changes of the sample due to thermal decomposition when using an accumulation-exposure time of 5 cycles of 30 s each. Five spots were randomly selected over the soot-loaded quartz filter to verify the homogeneity of the sample, and finally averaged to obtain a statistically relevant Raman spectrum. The standard deviation of the Raman spectra intensity in the first-order region was of the order of a few percent.

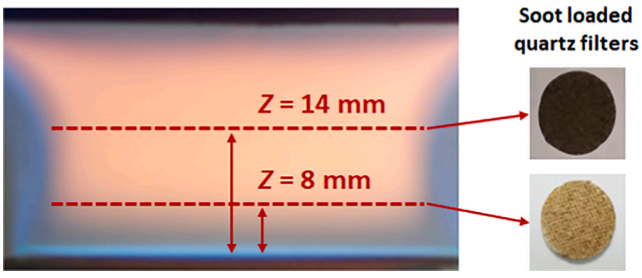

Fig. 1. Laminar premixed flame. The dashed red lines indicate the two sampling locations, corresponding to $Z = 8$ mm for just-nucleated soot particles and $Z = 14$ mm for aged/mature soot particles. (For interpretation of the references to colour in this figure legend, the reader is referred to the web version of this article.)

2.2. Quantum chemical methods

For each model molecule reported in this work we have carried out density functional theory (DFT) calculations including dispersion effects at the B3LYP/6-31G(d,p)-D3(BJ) level by using the Gaussian package [51]. The molecular structures of the monomers and dimers in gas phase were fully optimized with tight threshold to provide the reference structures that were subjected to the uniform expansion/contraction of the CC bond lengths (monomers) and π stacking distance (dimers) as a computationally convenient way to simulate the effects of thermal expansion. The details about the setup of the molecular structures used for the DFT calculations of the change of the G band associated to the change of the average CC bond length are provided in the Supplementary material.

The DFT calculations on graphene were carried out within periodic boundary conditions with the CRYSTAL17 code [52]. The B3LYP functional was adopted also in this case, and we have selected the 6-21G* basis set for carbon, as adapted for crystal calculations [53]. To ease the convergence of the self consistent field we have adopted a finite temperature smearing of the Fermi surface (kT = 0.001 hartree) and Fock matrix mixing (90%) with the Anderson scheme [54]. Due to the presence of long range interactions in graphene, we selected tight parameters for the truncation criteria for bielectronic integrals (TOLINTEG 13 13 13 1326) [54]. Furthermore, we also imposed accurate reciprocal space integration by adopting large shrinking factors (SHRINK 150 150) [54] and a supercell containing 6 carbon atoms, that was also described in [55]. The data reported in Table 1 were obtained from the calculation of the Γ point phonons in graphene structures with selected R_{CC} values (see Supplementary material).

3. Results

3.1. Temperature-dependent Raman spectra of soot (just-nucleated vs. grown aged/mature-particles)

The Raman spectrum of soot collected at 14 mm is reported in Fig. 2a. As expected in this kind of materials, the most evident Raman features in the spectral region ranging from 800 to 2200 cm^{-1} are the D and G bands, as indicated in Fig. 2a. The presence of defects in the sp^2 aromatic network activates the Raman D mode at ~1350 cm^{-1}. This is due to the A_1' in-plane stretching mode of C–C bonds that produce a collective breathing of alternate aromatic rings; the associated phonon is not found at q = 0 (Γ point) in the perfect hexagonal lattice, which is why it can be activated only in presence of symmetry breaking phenomena, such as disorder [56]. The G band at ~1600 cm^{-1} is associated with the Raman active E_{2g} in-plane C–C stretching vibration of the hexagonal graphene/graphite lattice [57]. On the high frequency side of the G band, there is a further contribution, not indicated in Fig. 2a. This band, located at about 1620 cm^{-1}, is named D' band in the graphene/graphite community, or D2 in a terminology introduced for soot by Sadesky et al. [24]. This terminology originates from the fact that this band is activated by disorder through a double resonance scattering of phonons in the graphitic lattice. Soot particles are mostly composed by sp^2 carbon arranged in polyaromatic units with a size of the order of 1 nm, showing heterogeneous molecular structures (*i.e.*, disordered). Because of this, the Raman selection rule of ordered crystalline materials, $q \approx 0$, in soot relaxes, and Raman optical phonons with wavenumber higher than that of the G band are also allowed. In the following, the G Raman band has been considered as a whole, without differentiating among the various contributions, and we have analysed the changes in the position of the maximum of the G band for increasing temperatures as shown in Fig. 2b and c.

Fig. 3 shows in the form of contour plots the variable temperature Raman spectra of the two soot samples, placed in a nitrogen inert atmosphere, with the temperature rising from 300 K to 525 K. Each Raman spectrum has been normalized to the maximum of the G band to ease the observation of changes in the spectral shape of this band, which is directly associated with the sp^2 content. The results obtained for the just-nucleated soot sample are shown in Fig. 3a, whereas the results for the aged/mature soot sample are shown in Fig. 3b. By increasing the temperature, some differences in the Raman spectra of the soot particles can be observed, yet such differences are much more clearly observable for the just-nucleated soot particles than for the mature soot particles.

For increasing temperatures in the investigated range the main spectral changes observed are: (i) the shift of both the D and G Raman bands towards lower wavenumbers, and (ii) a slight decrease in their bandwidth. This is evidenced in the plots of Fig. 4, where a magnified view of the G and D bands of just-nucleated soot sample is reported (see Fig. S2 in Supplementary material for the corresponding plot for the grown aged/mature soot sample).

It is worth to note that the relative intensity of the two Raman bands, I(D)/I(G), remains constant over the investigated temperature range. This result is consistent with reference [37]. Furthermore, it allows to conclude that the soot nanostructure is not likely to undergo chemical modifications due to pyrolytic reactions within the experimentally accessed temperature range. Indeed, it is well known that the I(D)/I(G) ratio correlates with the size of the aromatic domains, L_a, composing the carbon network [58,59]. This parameter is very sensitive to structural modification in soot, such as those caused by the use of too high laser power during the Raman measurements. The absence of variation of I(D)/I(G) with temperature in the examined range ensures that the structure is not graphitized by thermal annealing. For our soot samples I(D)/I(G) is equal to 0.8 ± 0.05 for the just-nucleated soot and 0.95 ± 0.05 for aged/mature soot. According to the known proportionality between I(D)/I(G) and L_a^2 valid for highly disordered carbon ($L_a^2 = 5.4 \bullet 10^{-2} \bullet E_L^4 \bullet I(D)/I(G)$ [59], where E_L is the energy of the incident photon) L_a is 1.15 nm for just-nucleated particles and 1.22 nm for the aged/mature soot, a result which is consistent with earlier investigations [60,61].

The evolution of the full width at half maximum (FWHM) of the main Raman bands at increasing temperature was studied in several earlier works and contrasting results were reported [37,40,41,47,48]. For the soot samples investigated here, the G and D bands show a slight narrowing for increasing temperature. However, due to the complexity of the Raman spectra of soots, this trend is affected by some uncertainty, whereas the most evident observation is the shift to lower frequencies of

Table 1
The position of the G-modes, ω_G, of the model species considered in this work, and the linear dependence of the G-modes on the CC bond length (expressed by the $\partial\omega_G/\partial R_{CC}$ parameter). The H/C ratios of the models are also given for reference. The reported ω_G^{eq} values are the wavenumbers (at equilibrium geometry) of the selected most intense G modes of the models considered here (Fig. 6). All the results reported in this table have been computed for isolated models (*i.e.*, not π-stacked dimers). The average value of $\partial\omega_G/\partial R_{CC}$ is -4.0×10^3 cm^{-1}/Å and its standard deviation is 0.2×10^3 cm^{-1}/Å.

Model	H/C	ω_G^{eq}(cm^{-1})	$\partial\omega_G/\partial R_{CC}$($10^3$ cm^{-1}/Å)
$C_{32}H_{14}$ molecule	0.44	1653	−4.0
(ovalene)		1668	−3.9
$C_{13}H_9^{\bullet}$ radical	0.69	1593	−3.5
(phenalenyl)		1607	−3.7
$C_{25}H_{13}^{\bullet}$ radical	0.52	1613	−3.9
		1673	−4.1
$C_{30}H_{17}^{\bullet}$ radical	0.57	1632	−4.0
		1689	−4.2
C_{60}	0.00	1623	−4.3
(fullerene)			
$C_{78}H_{26}$	0.33	1639	−4.0
(graphene-like molecule)		1650	−3.7
$C_{114}H_{30}$	0.26	1633	−3.9
(graphene-like molecule)		1667	−4.1
graphene	0.00	1616	−4.4

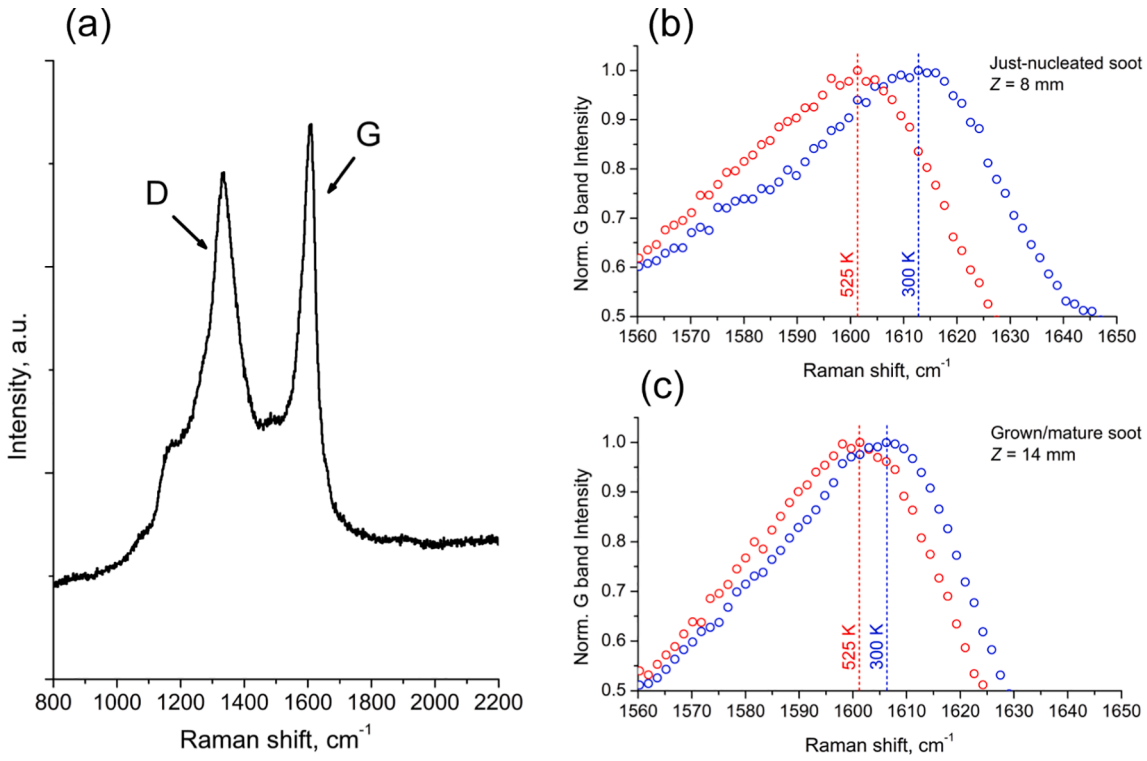

Fig. 2. (a) Raman spectrum of $Z = 14$ mm grown aged/mature soot recorded at room temperature with an excitation wavelength $\lambda_{exc} = 532$ nm. (b) and (c) are the G band position before and after thermal heating for the two soot samples. The dashed lines mark the position of the peak maximum.

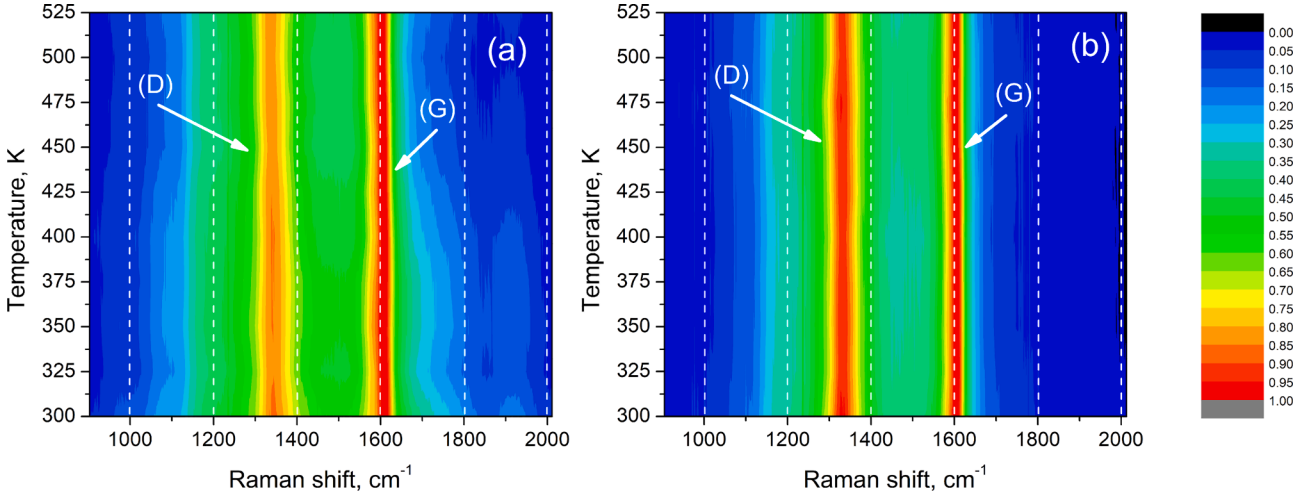

Fig. 3. Contour plots of the temperature-dependent Raman spectra in the spectral range 900–2000 cm^{-1} of soot samples heated in N_2 atmosphere from room temperature to 525 K. The Raman spectra have been recorded with stepwise temperature increases of 25 K. The contour plots have been obtained setting 20 iso-intensity levels from 0 to 1 without data smoothing. (a) just-nucleated soot nanoparticles; (b) grown aged/mature soot nanoparticles.

the G band of the two soot samples as temperature increases (Fig. 5). Several earlier works [37,39–50] report a good linear dependence of the position of the G band, ω_G, as a function of temperature, T, for many carbon-based material and many temperature ranges. We have therefore used a linear fitting of the G band position versus temperature to determine the temperature coefficient (χ_G) and the band position at $T = 0$ K (ω_0) from the slope and intercept of the fit function respectively. For both soot samples, the frequency of the G peak downshifts linearly with good coefficients of determination ($R^2 = 0.88$; 0.95), as shown in Fig. 5 where the data for increasing temperature together with the respective linear fit are reported.

As a result of the linear regression reported in Fig. 5, the just-nucleated soot particles show a temperature coefficient $\chi_G = -0.045 \pm 0.003$ cm^{-1}/K, and an intercept value $\omega_0 = 1622 \pm 1$ cm^{-1}, that are sensibly higher than the respective value obtained for the soot collected at higher residence time in flame ($Z = 14$ mm), corresponding to the mature/grown particles: $\chi_G = -0.021 \pm 0.003$ cm^{-1}/K and $\omega_0 = 1613 \pm 1$ cm^{-1}. We can notice that both samples present ω_0 larger than the typical position of graphite, 1580 cm^{-1}. This is a consequence of the disordered structure and small size of L_a that allows activation of higher-frequency phonons since the $q = 0$ selection rule relaxes [59]. In just nucleated soot the higher value of ω_0 is measured consistently with the smaller L_a.

To rationalize how soot maturity affects the temperature dependence

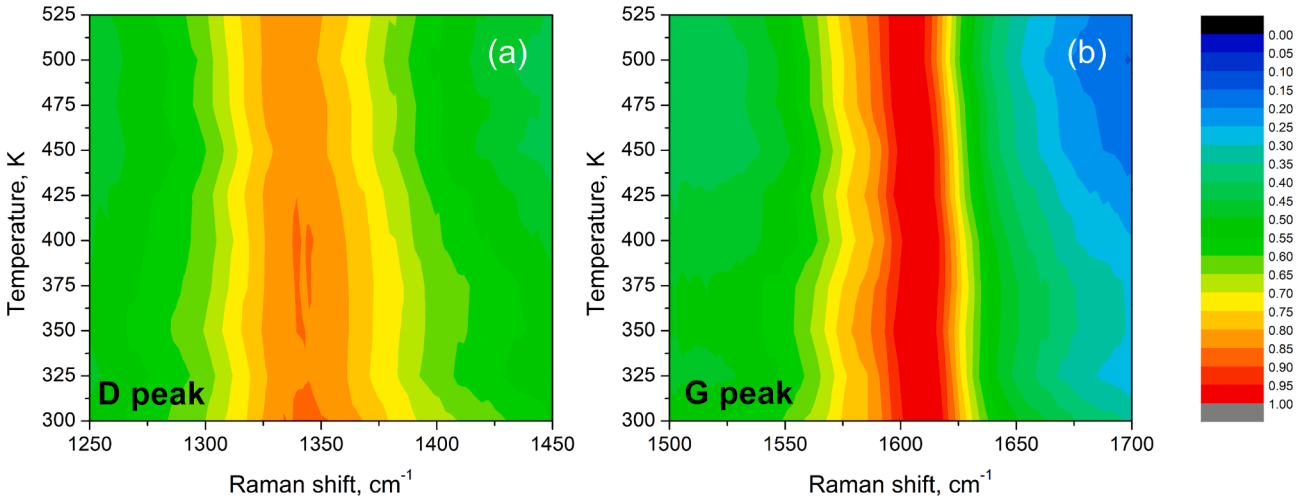

Fig. 4. Contour plots of the Raman spectra in the range 1250–1450 cm^{-1} of the D peak (left side) and 1500–1700 cm^{-1} of the G peak (right side) at various temperatures in the range 300–525 K for the just-nucleated soot particles.

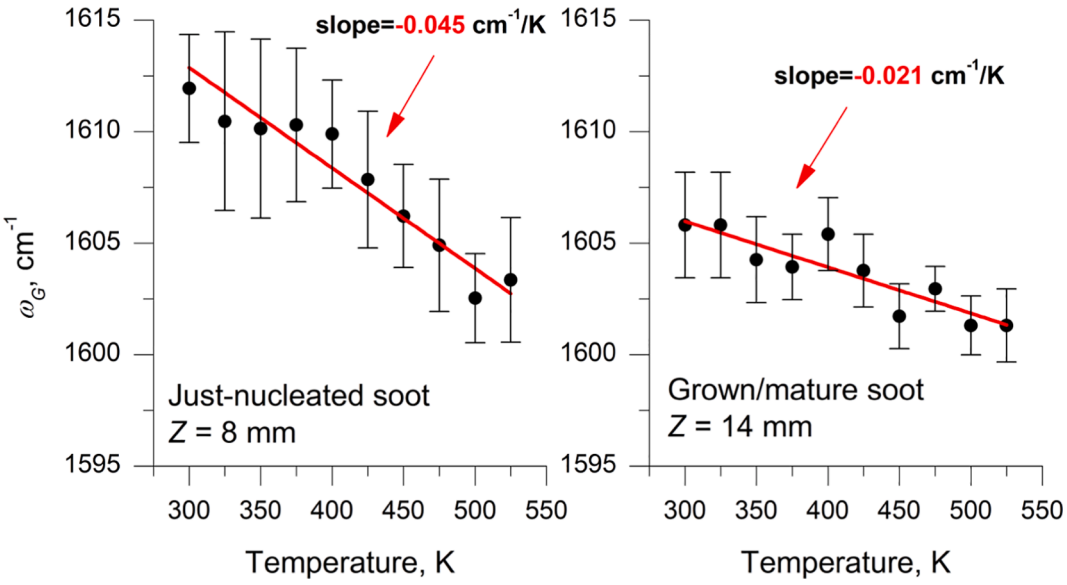

Fig. 5. Position of the G peak, ω_G, as function of the temperature in the range 300–525 K for the two samples in N_2 atmosphere. The red lines represent the obtained linear fit. (For interpretation of the references to colour in this figure legend, the reader is referred to the web version of this article.)

of the G band, we have developed a model based on results from density functional theory calculations. The model discussed below addresses the fundamental features of the G band by considering selected molecular structures that may be present in soot, and the perturbations that can be induced by the increase of temperature.

3.2. *Interpreting the temperature dependence of the G band of soot with a simple empirical model*

The temperature dependence of a Raman peak is the evidence of anharmonic effects that are at the basis of thermal expansion phenomena. Thermal effects in graphite and graphene have been modelled by density functional theory calculations through the quasi harmonic approximation [62], by which one considers a series of harmonic calculations of the normal modes of interest as a function of an imposed geometric distortion that describes the effects of the thermal expansion. Since we are interested in highly disordered materials for which the representation of phonons is problematic, it is not straightforward to follow the approach reported for graphene in [41], where the phonon anharmonicity, through phonon–phonon scattering contributions, leads to the detailed theoretical interpretation and quantitative modeling of the temperature dependence of the position of the G band. Therefore, we follow here a simple phenomenological approach, still based on the quasi harmonic picture, where the position of the G peak, ω_G, is anharmonically dependent upon the average CC bond lengths of the graphene molecule (R_{CC}) and the average π-stacking distance (d_π). Such geometric parameters are those that can capture most of the effects of thermal expansion, and have been also investigated in graphite through extensive and detailed experimental studies (see for instance reference [63] and the literature cited therein). Therefore, based on the expected dependence of ω_G upon the temperature-dependent average CC bond lengths and π-stacking distance, we can write:

$$\frac{\partial \omega_G}{\partial T} = \frac{\partial \omega_G(R_{CC}, d_\pi)}{\partial T} = \frac{\partial \omega_G}{\partial R_{CC}} \frac{\partial R_{CC}}{\partial T} + \frac{\partial \omega_G}{\partial d_\pi} \frac{\partial d_\pi}{\partial T} \quad (1)$$

Now, $\partial\omega_G/\partial T = \chi_G$ is the experimentally accessible quantity that is of central interest in this work. Eq. (1) clearly shows that from the measurements of $\partial\omega_G/\partial T$ one may hope to get information about the thermal

expansion of the sample ($\partial R_{CC}/\partial T$, $\partial d_\pi/\partial T$). Since thermal expansion involves the variation of both R_{CC} and d_π, it is required to assess the relative importance of the two terms in determining the measured value of $\partial\omega_G/\partial T$. To this aim, we consider the dimensionless r ratio between the two contributions to $\partial\omega_G/\partial T$ identified in Eq. (1):

$$r = \left[\frac{\partial\omega_G}{\partial d_\pi}\frac{\partial d_\pi}{\partial T}\right]\left[\frac{\partial\omega_G}{\partial R_{CC}}\frac{\partial R_{CC}}{\partial T}\right]^{-1} \quad (2)$$

As shown in the Supplementary material, the order of magnitude of the term $\left[\frac{\partial d_\pi}{\partial T}\right]\left[\frac{\partial R_{CC}}{\partial T}\right]^{-1}$ can be estimated based on the experimentally known ratio of the in-plane *vs*. out-of-plane thermal expansion of graphite. The expected values of $\partial\omega_G/\partial R_{CC}$ and $\partial\omega_G/\partial d_\pi$ can be assessed by density functional theory calculations on suitable molecular models. As described in the Supplementary material, such calculations have been performed for a series of model graphene molecules and selected dimers, as reported in Fig. 6a. From such calculations it resulted that r (Eq. (2)) is less than 10^{-2} in the ovalene dimer, whereas r is less than 10^{-1} in the dimers of the open shell/radical poly-cyclic aromatic species phenalenyl and $C_{30}H_{17}^{\bullet}$ that are representative of the radicals expected in soot inception [60,64,65]. Notably, $C_{30}H_{17}^{\bullet}$ was found in the ensemble of soot molecular constituents visualized by HR-AFM, and was named IS13 in Ref. [60].

Based on the computed low values of the r ratio, when interpreting the experimental $\partial\omega_G/\partial T$ data, we may therefore disregard the contributions that arise from the expansion of the π-stacking distance, and consider in Eq. (1) just the anharmonic effects caused by the CC bond length expansion:

$$\frac{\partial\omega_G}{\partial T} \approx \frac{\partial\omega_G}{\partial R_{CC}}\frac{\partial R_{CC}}{\partial T} \quad (3)$$

After the assessment of the negligible role of $\partial\omega_G/\partial d_\pi$ through the dimer models shown in Fig. 6a, we have carried out further density functional theory calculations of $\partial\omega_G/\partial R_{CC}$ for graphene and other representative radicals and molecules shown in Fig. 6b, namely $C_{25}H_{13}^{\bullet}$, $C_{78}H_{26}$, $C_{114}H_{30}$, and the C_{60} fullerene.

Table 1 collects the $\partial\omega_G/\partial R_{CC}$ values that have been obtained by all the DFT calculations described in this work. The data reported in Table 1 clearly show that the values of the $\partial\omega_G/\partial R_{CC}$ parameter are all rather independent on the model system, being it a closed shell, a radical, a pentagon-rich fullerene, or graphene itself. This leads to the remarkable consequence that for the sake of characterizing the temperature dependence of the Raman G band of soot, we may assume a representative average value of $\partial\omega_G/\partial R_{CC}$.

Now, since the in-plane thermal expansion coefficient can be written as $\alpha_a = R_{CC}^{-1}\partial R_{CC}/\partial T$, by plugging such definition of α_a into Eq. (3) we straightforwardly derive a way to characterize the in-plane thermal expansion of graphene molecules and related materials, based on the measured temperature dependence of the position of the G peak:

$$\alpha_a \approx \frac{1}{R_{CC}}\frac{\partial\omega_G/\partial T}{\partial\omega_G/\partial R_{CC}} = \frac{1}{R_{CC}}\frac{\chi_G}{\partial\omega_G/\partial R_{CC}} \quad (4)$$

This simple and remarkable result allows to directly correlate the

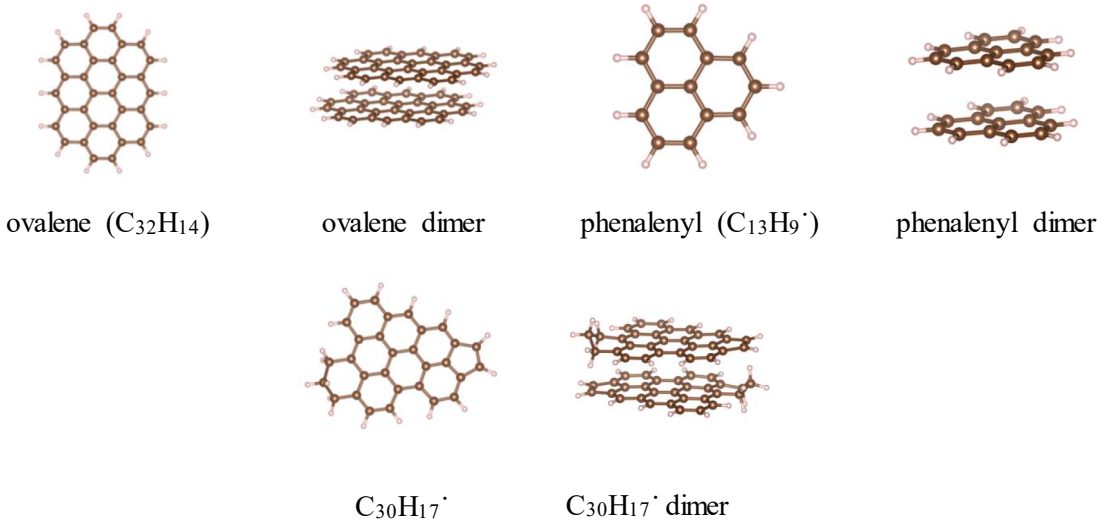

Fig. 6. (a, b) Representation of the set of model systems considered in this work, namely: ovalene ($C_{32}H_{14}$), phenalenyl ($C_{13}H_9^{\bullet}$), $C_{30}H_{17}^{\bullet}$, $C_{25}H_{13}^{\bullet}$, C_{60} (fullerene), $C_{78}H_{26}$, and $C_{114}H_{30}$. The panels (a) show the cases for which the density functional theory calculations on dimers have been considered, the panels (b) show others graphene-like molecules taken into account for density functional theory calculations (see Supplementary material).

observed temperature derivative of the position of the G peak (χ_G) to the thermal expansion of the sample along the in-plane direction (α_a). Indeed, this is possible thanks to the observed limited spread of $\partial\omega_G/\partial R_{CC}$ values across the representative diverse structures of the graphene moieties here considered that may form the disordered soot sample (Table 1).

4. Discussion

With the help of density functional theory calculations on selected model graphene-like molecules we have shown that the temperature dependence of the G band of soot ($\chi_G = \partial\omega_G/\partial T$) can be taken as a proxy of the thermal expansion coefficient of the soot sample along the in-plane direction (α_a). The experiments reported in Fig. 5 show for just-nucleated soot a $\partial\omega_G/\partial T$ value that is almost double ($-0.045\ cm^{-1}/K$) than the value measured on mature soot ($-0.021\ cm^{-1}/K$). This greater values of the thermal expansion α_a of incipient soot is consistent with a structure containing a larger amount of voids and defects that provide the space for easier thermal expansion of the disordered graphenic units. Therefore, the quantity $|\chi_G| \propto \alpha_a$ is expected to inversely correlate with the soot density. Consistently with this observation, recent experiments on pristine and ion-irradiated graphene [66] have shown that $\partial\omega_G/\partial T$ of graphene ($-0.0156\ cm^{-1}/K$) is significantly smaller than that of ion-irradiated graphene ($-0.0252\ cm^{-1}/K$). This has been interpreted as a greater thermal expansion of the lattice of ion-irradiated graphene, due to defects and vacancies. Remarkably, in the same work it was shown that $\partial\omega_G/\partial T$ is not affected by π-stacking since the same ω_G *vs.* T slopes were measured for graphene and few-layer graphene. This observation fully agrees with our determination of the negligible role in $\partial\omega_G/\partial T$ of the term depending on the π-stacking distance ($\partial\omega_G/\partial d_\pi$, see Supplementary material).

To confirm the interpretation of our results as correlated with the soot density, we have estimated the density for the two kind of particles herein investigated by following the procedure recently proposed by Michelsen [16], which relates the particle density to the H/C ratio. For the soot samples, an estimate of H/C was obtained, as already shown in our previous work [32,61], from the ratio between the fluorescence background and the intensity of the Raman G band and the correlation proposed by Casiraghi et al. [67]. The results are H/C = 0.43 for the just nucleated soot and H/C = 0.3 for the aged/mature soot. According to the relationship proposed by Michelsen [16] it results $\rho = 1.47$ for the just-nucleated soot and 1.60 g/cm^3 for the aged/mature soot, in agreement with the expectations derived from the quantum chemical models discussed above.

The dependence of thermal conductivity on the presence of impurities or defects, and thus on density, has been reported in many works on carbon materials such as graphite and carbon nanotubes [40,68–70]. The presence of voids or defects breaks the translational symmetry of the crystal lattice and increases phonon scattering events. More specifically, phonons are reflected, diffracted or refracted; the shorter is the phonon mean free path, the lower is the thermal conductivity [68]. The sensitivity of Raman spectroscopy to phonon mean free path makes it ideal for the analysis of thermal conductivity as well as disorder. In light of this, the higher value of the temperature coefficient χ_G measured in the just-nucleated soot sample *vs.* that measured in grown/mature soot, can be explained based on the different structural order expected in these two soot samples, the former being more amorphous/defective than the latter. Soot nanoparticles are, indeed, carbon nanomaterials whose molecular constituents are mainly PAHs. Recent studies made by high resolution atomic force microscopy [60,61], have clearly identified some of the main characteristics of the aromatic constituents including their average size, which is of the order of coronene to ovalene molecules, the presence of some aliphatic moieties, and the existence of molecules containing pentagonal-rings. Also, according to Raman spectroscopy, it was argued that the size of the aromatic constituents does not sensibly change between the just-nucleated particles and the grown/mature ones [12,61]. In previous works it was suggested that the major modifications occurring between these two kinds of particles are likely related to their structural organization. Furthermore, larger particles, also contain a lower H/C ratio and stronger interaction forces hold together the aromatic constituents. Possibly, chemical cross-linking occurs within the particles [18], as well as the formation of PAH stacks eventually bringing to the formation of a core–shell structure of the particles with a more graphitic shell surrounding an amorphous core [15–17] – particularly, as particle grows and matures with flame residence time. The possible occurrence of cross-linking between the aromatic constituents would lead to an increase in the thermal conductivity of the soot particles, and thus to a reduction in the heat capacity and thermal coefficient of the G band (χ_G). For instance, a strong increase in thermal conductivity was observed in amorphous polymer blends when weak van der Waals interactions were replaced by H bonds as low-mass and short chemical linker [70]. All of these structural changes, undergone by soot particles with aging, entail a stronger opposition to a small displacement from the equilibrium configuration, consistent with the lower slope of ω_G *vs.* T.

The comparison among the χ_G values measured in soot particles and other carbon-based materials is reported in Table 2. In addition to literature data, Table 2 also reports the results of the measurements of the temperature coefficient of coronene and fullerene-C_{60} crystalline powders, taken as representative planar and curved aromatic constituent structures that are expected to be present in soot particles. In the Figs. S3 and S4 of the Supplementary material the Raman spectra of coronene and C_{60} at room temperature are reported together with the temperature evolution of the position of the E_{2g} peak of coronene at 1594 cm^{-1} and the $H_g(8)$ peak of fullerene-C_{60} at 1574 cm^{-1}. The χ_G data reported in Table 2 cover a range spanning from the minimum value of $-0.011\ cm^{-1}/K$ found in C_{60} and HOPG to the maximum values of $-0.045\ cm^{-1}/K$ found in just nucleated soot. As discussed above, if one considers that χ_G is a proxy of the in-plane thermal expansion α_a, which is facilitated by the presence of voids/defects in the material, this situation fully makes sense: HOPG and C_{60} are characterized by excellent crystalline structures. For C_{60}, the equivalent of the in-plane thermal expansion of HOPG is the radial expansion of the C_{60} buckyball, which entails the deformation of a regular, defect-free, honeycomb structure. Therefore, not surprisingly, HOPG and C_{60} display similar and low values of χ_G that reflect the stronger opposition of such materials to changes in the CC bond length for a given thermal energy input. Interestingly, the coronene value is also low with respect to both just nucleated soot and grown mature soot. Although coronene can be considered, on average, as a molecule representative of the molecular units of soot, the higher tendency of soot to deform under heating with respect to a coronene crystal can be indicative of the larger disorder of the molecular arrangement in soot with respect to the coronene crystal.

5. Conclusions

We have investigated by temperature-dependent Raman spectroscopy two types of flame-formed soot particles, the first consisting of just-nucleated particles with average size of 3.5 nm, and the second made of grown/mature particles larger than 10 nm. The immediate aim was to evidence structural differences through the possible changes occurring in the Raman spectra, induced by the different thermal response of the particles. Our goal was also to provide the proof of concept for the use of this spectro-thermal method as a diagnostic tool for the determination of the maturity/graphitization level of soot particles. The introduction of a simple empirical model, supported by density functional theory calculations, has provided the interpretation of the experimental temperature dependence of the Raman G band of soot, and the rational for the possible applications of the spectro-thermal technique introduced here. The main results of our investigation can be summarized as follows.

Table 2
Temperature coefficients, χ_G, for different carbon materials. The excitation wavelength and temperature range used in the experiments are also reported.

Carbon sample	χ_G, cm^{-1}/K (intercept, ω_0, cm^{-1})	λ_{ext}, nm	Temperature range, K (heating method)	Ref.
Just-nucleated soot (Z = 8 mm)	−0.045 (1626)	532	300–775 (electrical/external)	This work
Grown mature soot (Z = 14 mm)	−0.021 (1612)	532	300–775 (electrical/external)	This work
Coronene	−0.019 (1594)	785	300–525 (electrical/external)	This work
Fullerene-C_{60}	−0.011 (1573)	785	300–525 (electrical/external)	This work
Pyrolytic Carbon	−0.013 (1585.8)	514.5	93–313 (laser)	Fischbach and Couzi [36]
Glass-like Carbon	−0.027	514.5	93–313 (laser)	Fischbach and Couzi [37]
Graphite (Lonza KS-5-75)	−0.03	514.5	302–873 (electrical/external)	Everall et al. [38]
HOPG/CHOPG*	−0.011/-0.028	514.5	260–647/258–815 (laser)	Tan et al. [39]
MWCNT	−0.028 (1661)	632.8**	380–820 (laser)	Huang et al. [41]
Activate Carbon	−0.027 (1615)	632.8**	380–820 (laser)	Huang et al. [41]
SWCNT (purified)	−0.038 (1606)	514.5	400–750 (laser and/or electrical/external)	Li et al. [42]
SWCNT	−0.0189 (1599)	514	299–773 (electrical/external)	Raravikar et al. [43]
graphene	−0.016 (1584)	488	83–373 (electrical/external)	Calizo et al. [45,46]
bilayer graphene	−0.015 (1582)	488	113–373 (electrical/external)	Calizo et al. [45,46]
HOPG	−0.011 (1584)	488	83–373 (electrical/external)	Calizo et al. [45]
graphene	−0.016	632.8	77–673 (electrical/external)	Late et al. [47]
Single-layer RGO	−0.029	632.8	77–673 (electrical/external)	Late et al. [47]
Six-layer graphene	−0.014	632.8	77–673 (electrical/external)	Late et al. [47]
GQDs/N-GQDs***	−0.0222/-0.0243	532	81–663 (electrical/external)	Thang et al. [48]

*Implanted with carbon (^{12}C) ions at ambient temperature.
**488.0 nm and 514.5 nm were also used giving the same results.
***Nitrogen-doped graphene quantum dots.

- Quantum chemical calculations justify the downshift of the G band of soot particles with increasing temperature as due to the elongation of the CC bonds: the model provides the interpretation of the temperature coefficient (χ_G) as a proxy of the in-plane thermal expansion coefficient within the layers of polycondensed rings that form the soot particles.
- The χ_G parameter is sensitive to the in-plane thermal deformation of the aromatic units within the particles, but it is not sensitive to deformations perpendicular to the aromatic planes and does not provide information on the staking order.
- The χ_G parameter is also sensitive to particle disorder and can be effectively employed for the analysis of the soot maturity: the difference in the measured temperature coefficient χ_G confirms a lower density for inception particles with respect to grown/mature soot.

CRediT authorship contribution statement

Mario Commodo: Conceptualization, Methodology, Writing – review & editing. **Gianluca Serra:** Data curation. **Serafina Bocchicchio:** Data curation. **Patrizia Minutolo:** Methodology, Writing – review & editing, Funding acquisition. **Matteo Tommasini:** Methodology, Formal analysis, Writing – review & editing, Funding acquisition. **Andrea D'Anna:** Writing – review & editing, Funding acquisition.

Declaration of Competing Interest

The authors declare the following financial interests/personal relationships which may be considered as potential competing interests: Patrizia Minutolo reports financial support was provided by Government of Italy Ministry of Education University and Research.

Acknowledgments

This research was conducted under the PRIN project 2017PJ5XXX: "MAGIC DUST". The work at University Federico II in Napoli was supported by the U.S. Air Force Office of Scientific Research (AFOSR) under grant number FA8655-21-1-7022.

Appendix A. Supplementary data

Supplementary data to this article can be found online at https://doi.org/10.1016/j.fuel.2022.124006.

References

[1] Kennedy IM. The health effects of combustion-generated aerosols. Proc Combust Inst 2007;31(2):2757–70.
[2] De Falco G, Terlizzi M, Sirignano M, Commodo M, D'Anna A, Aquino RP, et al. Human peripheral blood mononuclear cells (PBMCs) from smokers release higher levels of IL-1-like cytokines after exposure to combustion-generated ultrafine particles. Sci Rep 2017;7:43016.
[3] Bond TC, Doherty SJ, Fahey DW, Forster PM, Berntsen T, Deangelo BJ, et al. Bounding the role of black carbon in the climate system: a scientific assessment. J Geophys Res Atmos 2013;118:5380–552.
[4] Mulay MR, Chauhan A, Patel S, Balakrishnan V, Halder A, Vaish R. Candle soot: Journey from a pollutant to a functional material. Carbon 2019;144:684–712.
[5] D'Anna A. Combustion-formed nanoparticles. Proc Combust Inst 2009;32(1):593–613.
[6] Wang H. Formation of nascent soot and other condensed-phase materials in flames. Proc Combust Inst 2011;33(1):41–67.
[7] Michelsen HA. Probing soot formation, chemical and physical evolution, and oxidation: A review of in situ diagnostic techniques and needs. Proc Combust Inst 2017;36(1):717–35.
[8] Martin JW, Salamanca M, Kraft M. Soot inception: Carbonaceous nanoparticle formation in flames: Soot inception. *Prog Energy Combust Sci.* **2022**;88, art. no. 100956.
[9] Michelsen HA, Colket MB, Bengtsson P-E, D'Anna A, Desgroux P, Haynes BS, et al. A review of terminology used to describe soot formation and evolution under combustion and pyrolytic conditions. ACS Nano 2020;14(10):12470–90.
[10] Zhao B, Yang Z, Wang J, Johnston MV, Wang H. Analysis of soot nanoparticles in a laminar premixed ethylene flame by scanning mobility particle sizer. Aerosol Sci Technol 2003;37(8):611–20.
[11] Maricq MM. Size and charge of soot particles in rich premixed ethylene flames. Combust Flame 2004;137(3):340–50.
[12] Commodo M, De Falco G, Bruno A, Borriello C, Minutolo P, D'Anna A. Physicochemical evolution of nascent soot particles in a laminar premixed flame: From nucleation to early growth. Combust Flame 2015;162(10):3854–63.
[13] Carbone F, Attoui M, Gomez A. Challenges of measuring nascent soot in flames as evidenced by high-resolution differential mobility analysis. Aerosol Sci Technol 2016;50(7):740–57.

[14] Dobbins RA, Govatzidakis GJ, Lu W, Schwartzman AF, Fletcher RA. Carbonization rate of soot precursor particles. Combust Sci Technol 1996;121(1–6):103–21.
[15] Kholghy MR, Veshkini A, Thomson MJ. The core-shell internal nanostructure of soot - A criterion to model soot maturity. Carbon 2016;100:508–36.
[16] Michelsen HA. Effects of maturity and temperature on soot density and specific heat. Proc Combust Inst 2021;38(1):1197–205.
[17] Botero ML, Sheng Y, Akroyd J, Martin J, Dreyer JAH, Yang W, et al. Internal structure of soot particles in a diffusion flame. Carbon 2019;141:635–42.
[18] Pascazio L, Martin JW, Botero ML, Sirignano M, D'Anna A, Kraft M. Mechanical properties of soot particles: the impact of crosslinked polycyclic aromatic hydrocarbons. Combust Sci Technol 2021;193(4):643–63.
[19] Minutolo P, Gambi G, D'Alessio A. The optical band gap model in the interpretation of the UV-visible absorption spectra of rich premixed flames. Symp (Int) Combust 1996;26(1):951–7.
[20] Liu C, Singh AV, Saggese C, Tang Q, Chen D, Wan K, et al. Flame-formed carbon nanoparticles exhibit quantum dot behaviors. Proc Natl Acad Sci USA 2019;116 (26):12692–7.
[21] Kelesidis GA, Bruun CA, Pratsinis SE. The impact of organic carbon on soot light absorption. Carbon 2021;172:742–9.
[22] De Falco G, Mattiello G, Commodo M, Minutolo P, Shi X, D'Anna A, et al. Electronic band gap of flame-formed carbon nanoparticles by scanning tunneling spectroscopy. Proc Combust Inst 2021;38(1):1805–12.
[23] Camacho J, Tao Y, Wang H. Kinetics of nascent soot oxidation by molecular oxygen in a flow reactor. Proc Combust Inst 2015;35(2):1887–94.
[24] Sadezky A, Muckenhuber H, Grothe H, Niessner R, Pöschl U. Raman microspectroscopy of soot and related carbonaceous materials: Spectral analysis and structural information. Carbon 2005;43(8):1731–42.
[25] Lapuerta M, Oliva F, Agudelo JR, Stitt JP. Optimization of Raman spectroscopy parameters for characterizing soot from different diesel fuels. Combust Sci Technol 2011;183(11):1203–20.
[26] Herdman JD, Connelly BC, Smooke MD, Long MB, Miller JH. A comparison of Raman signatures and laser-induced incandescence with direct numerical simulation of soot growth in non-premixed ethylene/air flames. Carbon 2011;49 (15):5298–311.
[27] Seong HJ, Boehman AL. Evaluation of Raman parameters using visible Raman microscopy for soot oxidative reactivity. Energy Fuels 2013;27(3):1613–24.
[28] Minutolo P, Commodo M, Santamaria A, De Falco G, D'Anna A. Characterization of flame-generated 2-D carbon nano-disks. Carbon 2014;68:138–48.
[29] Commodo M, Joo PH, De Falco G, Minutolo P, D'Anna A, Gülder ÖL. Raman spectroscopy of soot sampled in high-pressure diffusion flames. Energy Fuels 2017; 31(9):10158–64.
[30] Commodo M, Karataş AE, De Falco G, Minutolo P, D'Anna A, Gülder ÖL. On the effect of pressure on soot nanostructure: A Raman spectroscopy investigation. Combust Flame 2020;219:13–9.
[31] Commodo M, De Falco G, Minutolo P, D'Anna A. Structure and size of soot nanoparticles in laminar premixed flames at different equivalence ratios. Fuel 2018;216:456–62.
[32] Commodo M, Picca F, Vitiello G, De Falco G, Minutolo P, D'Anna A. Radicals in nascent soot from laminar premixed ethylene and ehtylene-benzene flames by electron paramagnetic resonance spectroscopy. Proc Combust Inst 2021;38: 1487–95.
[33] Salamanca M, Botero ML, Martin JW, Dreyer JAH, Akroyd J, Kraft M. The impact of cyclic fuels on the formation and structure of soot. Combust Flame 2020;219: 1–12.
[34] Bonpua J, Yagües Y, Aleshin A, Dasappa S, Camacho J. Flame temperature effect on sp2 bonds on nascent carbon nanoparticles formed in premixed flames ($T_{f,\ max} >$ 2100 K): A Raman spectroscopy and particle mobility sizing study. Proc Combust Inst 2019;37(1):943–51.
[35] Bonini N, Lazzeri M, Marzari N, Mauri F. Phonon anharmonicities in graphite and graphene. Phys Rev Lett 2007;99(17):176802.
[36] Sun Z, Yuan K, Chang Z, Zhang X, Qin G, Tang D. Efficient thermal conductivity modulation by manipulating interlayer interactions: A comparative study of bilayer graphene and graphite. J Appl Phys 2019;126(12):125104.
[37] Fischbach DB, Couzi M. Temperature dependence of Raman scattering by disordered carbon materials. Carbon 1986;24(3):365–9.
[38] Zouboulis ES, Grimsditch M. Raman scattering in diamond up to 1900 K. Phys Rev B Condens Matter 1991;43(15):12490–3.
[39] Everall NJ, Lumsdon J, Christopher DJ. The effect of laser-induced heating upon the vibrational raman spectra of graphites and carbon fibres. Carbon 1991;29(2): 133–7.
[40] Tan P, Deng Y, Zhao Q, Cheng W. The intrinsic temperature effect of the Raman spectra of graphite. Appl Phys Lett 1999;74(13):1818–20.
[41] Liu H-N, Cong X, Lin M-L, Tan P-H. The intrinsic temperature-dependent Raman spectra of graphite in the temperature range from 4K to 1000K. Carbon 2019;152: 451–8.
[42] Huang F, Yue KT, Tan P, Zhang S-L, Shi Z, Zhou X, et al. Temperature dependence of the Raman spectra of carbon nanotubes. J Appl Phys 1998;84(7):4022–4.
[43] Li HD, Yue KT, Lian ZL, Zhan Y, Zhou LX, Zhang SL, et al. Temperature dependence of the Raman spectra of single-wall carbon nanotubes. App Phys Lett 2000;76(15): 2053–5.
[44] Raravikar NR, Keblinski P, Rao AM, Dresselhaus MS, Schadler LS, Ajayan PM. Temperature dependence of radial breathing mode Raman frequency of single-walled carbon nanotubes. Phys Rev B Condens 2002;66(23):2354241–9.
[45] Ci L, Zhou Z, Song L, Yan X, Liu D, Yuan H, et al. Temperature dependence of resonant Raman scattering in double-wall carbon nanotubes. App Phys Lett 2003; 82(18):3098–100.
[46] Calizo I, Miao F, Bao W, Lau CN, Balandin AA. Variable temperature Raman microscopy as a nanometrology tool for graphene layers and graphene-based devices. App Phys Lett 2007;91(7):071913.
[47] Calizo I, Balandin AA, Bao W, Miao F, Lau CN. Temperature dependence of the Raman spectra of graphene and graphene multilayers. Nano Lett 2007;7(9): 2645–9.
[48] Late DJ, Maitra U, Panchakarla LS, Waghmare UV, Rao CNR. Temperature effects on the Raman spectra of graphenes: Dependence on the number of layers and doping. J Condens Matter Phys 2011;23(5):055303.
[49] Thang PN, Hung LX, Thuan DN, Yen NH, Hien NTT, Hanh VTH, et al. Temperature-dependent Raman investigation and photoluminescence of graphene quantum dots with and without nitrogen-doping. J Mater Sci 2021;56(8):4979–90.
[50] Rosenburg F, Ionescu E, Nicoloso N, Riedel R. High-temperature Raman spectroscopy of nano-crystalline carbon in silicon oxycarbide. Materials 2018;11 (1):93.
[51] Frisch M.J., Trucks, G.W., Schlegel, H.B., Scuseria, G.E., Robb, M.A., Cheeseman, J. R., Scalmani, G., Barone, V., Mennucci, B., Petersson, G.A., Nakatsuji, H., Caricato, M., Li, X., Hratchian, H.P., Iz-maylov, A.F., Bloino, J., Zheng, G., Sonnenberg, J.L., Hada, M., Ehara, M., Toyota, K., Fukuda, R., Hasegawa, J., Ishida, M., Nakajima, T., Honda, Y., Kitao, O., Nakai, H., Vreven, T., Montgomery, J.A., Jr., Per-alta, J.E., Ogliaro, F., Bearpark, M., Heyd, J.J., Brothers, E., Kudin, K.N., Staroverov, V.N., Kobayashi, R., Normand, J., Raghavachari, K., Rendell, A., Burant, J.C., Iyengar, S. S., Tomasi, J., Cossi, M., Rega, N., Millam, J.M., Klene, M., Knox, J.E., Cross, J.B., Bakken, V., Adamo, C., Jaramillo, J., Gomperts, R., Stratmann, R.E., Yazyev, O., Austin, A.J., Cammi, R., Pomelli, C., Ochterski, J.W., Martin, R.L., Morokuma, K., Zakrzewski, V.G., Voth, G.A., Salvador, P., Dannenberg, J.J., Dapprich, S., Daniels, A.D., Farkas, Ö., Foresman, J.B., Ortiz, J.V., Cioslowski, J., Fox D.J. Gaussian09 revisionD. 01. Gaussian Inc. Wallingford CT **2009**.
[52] Dovesi R, Erba A, Orlando R, Zicovich-Wilson CM, Civalleri B, Maschio L, et al. Quantum-mechanical condensed matter simulations with crystal. WIREs Comput Mol Sci 2018;8(4):e1360.
[53] Catti M, Pavese A, Dovesi R, Saunders VR. Static lattice and electron properties of MgCO3 (magnesite) calculated by ab initio periodic hartree-fock methods. Phys Rev B 1993;47:9189–98.
[54] Dovesi R, Saunders VR, Roetti C, Orlando R, Zicovich-Wilson CM, Pascale F, Civalleri B, Doll K, Harrison NM, Bush IJ, D'Arco P, Llunell M, Causà M, Noël Y, Maschio L, Erba A, Rerat M, Casassa S, Crystal17 user's manual, **2017**.
[55] Tommasini M, Di Donato E, Castiglioni C, Zerbi G. Relaxing the graphite lattice along critical directions: The effect of the electron–phonon coupling on the π electron band structure. Chem Phys Lett 2005;414(1):166–73.
[56] Castiglioni C, Negri F, Rigolio M, Zerbi G. Origin of the D line in the Raman spectrum of graphite: A study based on Raman frequencies and intensities of polycyclic aromatic hydrocarbon molecules. J Chem Phys 2001;115:3769–78.
[57] Ferrari AC, Robertson J, Castiglioni C, Tommasini M, Zerbi G. Raman spectroscopy of polyconjugated molecules and materials: Confinement effect in one and two dimensions. Phil Trans R Soc Lond A 2004;362(1824):2425–59.
[58] Martins Ferreira EH, Moutinho MVO, Stavale F, Lucchese MM, Capaz RB, Achete CA, et al. Evolution of the Raman spectra from single-, few-, and many-layer graphene with increasing disorder. Phys Rev B Condens 2010;82(12):125429.
[59] Ferrari AC, Basko DM. Raman spectroscopy as a versatile tool for studying the properties of graphene. Nat Nanotechnol 2013;8(4):235–46.
[60] Commodo M, Kaiser K, De Falco G, Minutolo P, Schulz F, D'Anna A, et al. On the early stages of soot formation: Molecular structure elucidation by high-resolution atomic force microscopy. Combust Flame 2019;205:154–64.
[61] Schulz F, Commodo M, Kaiser K, De Falco G, Minutolo P, Meyer G, et al. Insights into incipient soot formation by atomic force microscopy. Proc Combust Inst 2019; 37(1):885–92.
[62] Mounet N, Marzari N. First-principles determination of the structural, vibrational and thermodynamic properties of diamond, graphite, and derivatives. Phys Rev B Condens Matter 2005;71(20):1–14.
[63] Zorzi JE, Perottoni CA. Thermal expansion of graphite revisited. Comput Mater Sci 2021;199:110719.
[64] Gentile FS, Picca F, De Falco G, Commodo M, Minutolo P, Causà M, et al. Soot inception: A DFT study of σ and π dimerization of resonantly stabilized aromatic radicals. Fuel 2020;279:118491. https://doi.org/10.1016/j.fuel.2020.118491.
[65] Martin JW, Pascazio L, Menon A, Akroyd J, Kaiser K, Schulz F, et al. π-Diradical aromatic soot precursorsin flames. J Am Chem Soc 2021;143(31):12212–9.
[66] Yang M, Wang L, Qiao X, Liu Y, Liu Y, Shi Y, et al. Temperature dependence of G and D' phonons in monolayer to few-layer graphene with vacancies. Nanoscale Res Lett 2020;15(1):189.
[67] Casiraghi C, Piazza F, Ferrari AC, Grambole D, Robertson J. Bonding in hydrogenated diamond-like carbon by Raman spectroscopy. Diam Relat Mater 2005;14(3-7):1098–102.
[68] Burger N, Laachachi A, Ferriol M, Lutz M, Toniazzo V, Ruch D. Review of thermal conductivity in composites: Mechanisms, parameters and theory. Prog Polym Sci 2016;61:1–28.
[69] Kim YA, Kamio S, Tajiri T, Hayashi T, Song SM, Endo M, et al. Enhanced thermal conductivity of carbon fiber/phenolic resin composites by the introduction of carbon nanotubes. Appl Phys Lett 2007;90(9):093125.
[70] Kim G-H, Lee D, Shanker A, Shao L, Kwon MS, Gidley D, et al. High thermal conductivity in amorphous polymer blends by engineered interchain interactions. Nat Mater 2015;14(3):295–300.